

---

This is an electronic reprint of the original article.  
This reprint may differ from the original in pagination and typographic detail.

Tomin, Oleksii; Yazdani, Maryam Roza

## Production and characterization of porous magnetic biochar : before and after phosphate adsorption insights

*Published in:*  
Journal of Porous Materials

*DOI:*  
[10.1007/s10934-022-01217-1](https://doi.org/10.1007/s10934-022-01217-1)

Published: 01/06/2022

*Document Version*  
Publisher's PDF, also known as Version of record

*Published under the following license:*  
CC BY

*Please cite the original version:*  
Tomin, O., & Yazdani, M. R. (2022). Production and characterization of porous magnetic biochar : before and after phosphate adsorption insights. *Journal of Porous Materials*, 29(3), 849-859.  
<https://doi.org/10.1007/s10934-022-01217-1>



# Production and characterization of porous magnetic biochar: before and after phosphate adsorption insights

Oleksii Tomin<sup>1</sup> · Maryam Roza Yazdani<sup>2</sup>

Accepted: 19 February 2022 / Published online: 1 March 2022  
© The Author(s) 2022

## Abstract

The modification process of biochars enables different advantages including enhanced adsorption properties for different pollutants. Herein, porous magnetic biochars (PMB) were successfully produced from softwood biomass through a two-step pyrolysis process together with  $\text{FeCl}_3$  modification. The effect of production temperature on adsorption was studied at 200 or 300 °C, followed by iron salt modification and subsequent pyrolysis at 600 or 800 °C. Biochars were characterized before and after phosphate adsorption via various characterization methods to acquire structural, elemental, and morphological properties of the adsorbent. The effects of phosphate concentration, contact time, and temperature on the adsorption process were examined in the batch mode. The characterization showed embedded iron oxide crystals of 23 nm within the biochar structure with a magnetic strength of 38.9 emu/g, which can assist the separation process of the powdered adsorbent from the aqueous medium. The surface area of the PMB was measured as 93 m<sup>2</sup>/g and 0.002 cm<sup>3</sup>/g pore volume. PMB showed complete removal (100%) of phosphate at the lower concentration (5 mg/l P). At higher concentration (25 mg/l P), the biochar prepared under 200/800 °C showed the highest removal (30%). The adsorption was enhanced with time (optimal 3 h) and temperature, which shows endothermic chemisorption following Langmuir isotherm and Pseudo-second order kinetic models. The desorption study suggested the slow release of phosphate from the spent adsorbent and potential reuse for soil enhancement. These results point towards the sustainable use of PMB as an effective and magnetically recyclable adsorbent for phosphate removal and reclaim.

**Keywords** Adsorption · Characterization · Chemical activation · Porous magnetic biochar · Phosphate removal · Water treatment

## 1 Introduction

Biochars are carbonized biomass, commonly used for soil and water treatment purposes. They have become popular as adsorbents thanks to their high porosity, adsorptive surface functionality, and the possibility of tailoring their properties for enhanced removal of specific pollutants [1–3]. In addition to promising adsorptive properties, biochar is relatively

easy and cost-effective to produce from locally available biomass sources. Depending on the demand, it can be made by using large- or small-scale pyrolysis units in production facilities which can be situated both near biomass sources and near application points. Recent studies confirm effective adsorption of pharmaceuticals [4], organic matters [1], and heavy metals [5] with biochar produced from locally available biomass.

Biochars result from the thermal treatment of biomass in a limited oxygen atmosphere. The production method, and conditions as well as the type of biomass affect the final properties of the biochars. The most common methods for biochar production are fast pyrolysis, slow pyrolysis, and hydrothermal carbonization (so-called hydrochar) [6]. The pyrolysis can be performed at different temperatures. For example, low-temperature pyrolysis leads to porous biochars with low oxygen and hydrogen content, while high temperatures result in enhanced surface area,

✉ Oleksii Tomin  
oleksii.tomin@aalto.fi

✉ Maryam Roza Yazdani  
roza.yazdani@aalto.fi

<sup>1</sup> Department of Built Environment, School of Engineering, Aalto University, P.O. Box 15200, 00076 Aalto, Finland

<sup>2</sup> Department of Mechanical Engineering, School of Engineering, Aalto University, P.O. Box 14400, 00076 Aalto, Finland

hydrophobicity, and porosity [6]. Furthermore, physical or chemical activation can be applied to improve biochar's properties. Activation oxidizes the surface of the biochar and introduces further functional groups in its structure [7]. Obtained functional groups allow the specific interactions on the adsorbent surface, e.g. electrostatic attraction, which results in more effective adsorption of pollutants from water [8]. Biochars with such properties can compete with conventional activated carbons, which are often developed from the fossil-based origin, for water treatment purposes [1].

A variety of biomass sources can be utilized for biochar production, including forestry and agricultural by-products e.g. bark, rice husk, straws, algae [9, 10], as well as abundant woody biomass. Spruce is a widespread softwood species, locally available in many countries, particularly Finland. This softwood species naturally provides high porosity, which enables the production of highly porous biochars [11]. Furthermore, its availability in large amounts and its high lignocellulosic content make spruce cost-effective biomass for biochar production [12]. To this end, we intend to develop a chemically activated biochar from spruce for the adsorption of phosphate. The motivation behind the chemical activation is to improve the porosity and surface functionality towards higher adsorption of phosphate and recyclability of the adsorbent for further use.

Phosphate is increasingly utilized in anthropogenic activities, mainly as organic fertilizer, due to the growing demand for agricultural and livestock production [13]. The excess amount of phosphate can end up in natural water bodies, leading to the increased content of nutrients in the water and consequent eutrophication, followed by changes in the biological indicators. For example, the qualitative and quantitative composition of fish is reduced due to the intensive reproduction of parasitic organisms and the sanitary and epidemiological situation deteriorates. The diseases of aquatic inhabitants also intensify [14]. Thus, it is crucial to treat the phosphate-containing water before its discharge into the environment. The conventional way to remove phosphate from wastewater is through chemical precipitation or coagulation [15]. Such methods, however, have led to the generation of a large amount of sludge, subsequent sludge management, and nutrient loss issues. The removal and recovery of phosphate via adsorption with biochars, on the other hand, have shown promising results [16]. As a tertiary treatment step, passing the effluent through a biochar-based media not only removes the excess phosphate from the water but also allows collecting this limiting element for reuse. As phosphate is a finite resource, saving and recycling it back to use is a significant environmental target. After exhaustion, phosphate-loaded biochar can be desorbed for multiple reuses of the adsorbent or be used directly as a soil amendment for agricultural purposes [17]. Additionally, the solid

carbon powder loaded with nutrients can be easily separated from water through magnetic properties.

This study aims to fabricate functionalized magnetic biochars through chemical activation and use it for the adsorption of phosphate. An iron salt is selected as the activator to create iron-based surface functional groups that provide a high affinity for phosphate. This further enables magnetic properties for the biochar, which can assist the separation process of the biochar powder from the water after the treatment. Spruce, a common product of forestry in Finland, is selected as the local source of biomass. A two-step pyrolysis process is performed to produce the biochars under different temperatures and to identify suitable production conditions. Conventionally biochar is produced via a one-step pyrolysis process which has been reported to be less effective than two-step pyrolysis in creating desired adsorptive properties [1]. The developed adsorbent is further characterized via scanning electron microscopy (SEM), energy dispersive X-ray (EDX), Brunauer, Emmett, and Teller (BET) surface area and porosity, Fourier-transform infrared spectroscopy (FTIR), and X-ray diffraction (XRD) methods before and after adsorption of phosphate. Moreover, the magnetic strength of the pristine and loaded biochars is measured with a vibrating sample magnetometer. To the best of our knowledge, there are limited studies on such characterization of phosphate-loaded biochar. In addition, a desorption study is performed to understand the phosphate release from the spent adsorbent and the possibilities of phosphorous reclamation.

## 2 Materials and methods

### 2.1 Biochar production

Biochars were produced from spruce sawdust, which was previously prepared and sieved through a 1 mm sieve and then stored in closed packages in a cold room before pyrolysis.  $\text{FeCl}_3 \cdot 6\text{H}_2\text{O}$  (Merck) was used as a chemical activator.

Four types of porous magnetic biochars (PMB) were prepared via two-step pyrolysis with the chemical activation process according to our previous research on pinecone [1]. Firstly, spruce sawdust was pyrolyzed at two different low temperatures: 200 or 300 °C for 15 min under nitrogen atmosphere in Naber N60/HR furnace. Then, biochar from the first step was modified with an iron salt, via mixing the chemical solution in a 1/2 ratio of biochar/activator for 2 h. The mixture was dried for 24 h under 105 °C and finally pyrolyzed again under the nitrogen atmosphere at high temperatures 600 or 800 °C. Obtained biochars were named according to the temperature of preparation at the first and second step of pyrolysis, as A1 (200/600 °C), A2 (200/800 °C), B1 (300/600 °C), and B2 (300/800 °C).

Additionally, two reference biochars without the activation were produced for comparison with the two-step pyrolysis method. The one-step pyrolysis biochar without activation was prepared under 300 °C (R3) and the two-step pyrolysis biochar without activation was prepared under 600 °C (R6). After preparation, all products were rinsed with 0.1 M HCl and reverse osmosis water until a neutral pH was obtained and dried at 105 °C overnight.

## 2.2 Biochar characterization

To study the functional properties of the PMB, such as porosity, morphology, composition before and after the adsorption of phosphate, the samples were characterized via SEM–EDX, BET surface area and porosity, FTIR, and XRD. The SEM–EDX analysis was performed on the JEOL JSM-7500FA analytical field Emission scanning electron microscope using 10 µA probe current and 10 kV acceleration voltage. For sample preparation, biochar was fixed on a metal stub with carbon tape and no coating was applied. For BET measurement, the samples were first dried overnight and put in a Micromeritics FlowPrep 060 sample preparation system for degasification under 200 °C for 3 h with flowing N<sub>2</sub> gas. The BET was measured by a Micromeritics TriStar II 3020 automated gas adsorption analyzer. The FTIR analysis was performed on a PerkinElmer Spectrum Two FT-IR Spectrometer with a high-performance LiTaO<sub>3</sub> MIR detector. The spectra were recorded at room temperature within the range of 600–4000 cm<sup>−1</sup> under 4 repetitious scans with 4 cm<sup>−1</sup> resolution. The XRD measurement was performed on a Rigaku SmartLab X-ray diffractometer. The XRD profiles were analyzed and the peaks were identified using Malvern Panalytical HighScore Plus software. The magnetization curves were measured using a vibrating sample magnetometer (VSM) (Quantum Design DynaCool Physical Property Measurement System) at 300 K.

## 2.3 Adsorption batch experiments

Phosphate removal by the PMB was studied via adsorption batch experiments. A stock solution with a concentration of 1000 mg/l was made by weighing an accurate amount of potassium dihydrogen phosphate (KH<sub>2</sub>PO<sub>4</sub>, Merck) and dissolving it in reverse osmosis water. Different dilutions were prepared daily before each adsorption set.

All batch experiments were conducted on a shaker at the speed of 180 rpm using 50 ml phosphate solutions and 2 g/l of the magnetic adsorbent. The pH was not adjusted. After the required contact time, the solutions were filtered with Sartorius Minisart 45 µm filters and analyzed for final phosphate concentration. The determination of phosphate was carried out with the Discrete analyzer Skalar BlueVision, using method PO<sub>4</sub>low: 5–500 µg/l P and method PO<sub>4</sub>high:

0.5–5 mg/l P, in compliance with ISO 15923-1. The effect of phosphate concentration on the removal efficiency was explored from 5 to 25 mg/l P upon 3 h contact time. The effect of contact time was studied at different time intervals between 30 min and 8 h at 10 mg/l P concentration. Phosphate solutions with an initial concentration of 10 mg/l P were used to study the effect of temperature on the adsorption process at 10, 22 (room temperature), 30, 40 and 50 °C upon 3 h of contact time and with no pH adjustment. All the batch experiments were carried out in two replicates. The percent of phosphate removal efficiency from the solution was calculated via the equation:

$$\text{Removal (\%)} = \left( \frac{C_0 - C_1}{C_0} \right) \times 100, \quad (1)$$

where  $C_0$  is the initial concentration of the solution,  $C_1$  is the final concentration after adsorption.

## 2.4 Desorption study

To study the desorption ability of PMB, the adsorption–desorption study was performed. The study consisted of 3 consecutive adsorption–desorption cycles. A known amount of biochar was added in a 25 mg/l P phosphate solution for 3 h. After 3 h of mixing, the sample was collected and dried overnight in an oven at 105 °C. The spent biochar was added into acidified reverse osmosis water (pH 2) and agitated for different desorption times such as 30 min, 1 h, 3 h, 6 h, and 8 h. The amount of released phosphate was measured in obtained solutions. After the cycle biochar was collected, washed with reverse osmosis water, and dried in the oven overnight at 105 °C to be used in the next cycle.

The percent of desorption was calculated with the equation:

$$\text{Desorption (\%)} = \left( \frac{C_{\text{ad}} - C_{\text{ds}}}{C_{\text{ad}}} \right) \times 100, \quad (2)$$

where  $C_{\text{ad}}$  is the amount of phosphate adsorbed on the biochar surface,  $C_{\text{ds}}$  is the concentration of phosphate in reverse osmosis water after desorption.

# 3 Results and discussion

## 3.1 Characterization

The yield of the PMB after the two-step pyrolysis process was determined and shown in Fig. 1. Biochars produced at 200, and 300 °C (first step pyrolysis) showed a constant decrease in yield with an increase of second step pyrolysis temperature (600 and 800 °C) from 43 to 12% and from 22 to 9% respectively. Generally, increasing the pyrolysis

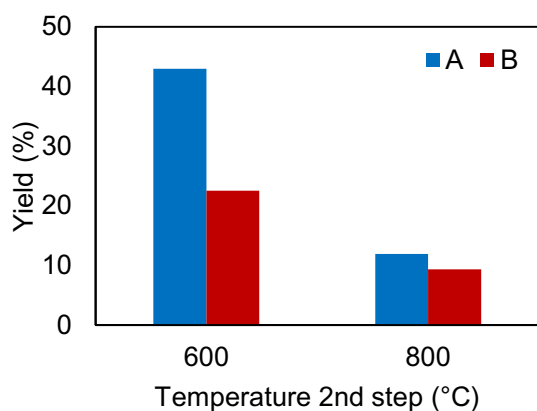


**Fig. 1** Comparison of the PMB yield produced at different temperatures. Different colors represent different temperatures in the first step of pyrolysis (Color figure online)

temperatures resulted in a lower PMB yield, which is consistent with previously reported results, based on research with various biomass, including pinewood [18, 19]. The main reason for the decline in PMB yield is mainly due to the thermal decomposition of cellulose and hemicellulose followed by the conversion of other organic components with increasing the pyrolysis temperature. The average solid yield for biochars produced at temperatures 500–900 °C without chemical impregnation was previously reported to be around 30–37% [6]. The chemical activation at high pyrolysis temperatures usually leads to lower carbon yield due to the catalytic influence of the chemical activators, which results in higher porosity in the produced carbon.

SEM imaging showed the highly porous structure of the biochar as well as the presence of crystalline ferric compounds within the biochar structure (Fig. 2a). This indicates the development of a hierarchical porous carbon structure hosting magnetic ferric particles which can act as the active sites for phosphate removal. The SEM image of the biochar surface after the phosphate adsorption (Fig. 2b) revealed changes in the surface morphology, confirming the formation of the phosphate-ferric complexation coverage on the surface. The crystals of ferric oxide are transformed into smooth-shaped particles, which suggests the occurrence of phosphate-iron complexation/precipitation on the carbon surface. Previously, engineered biochar containing nano-sized AlOOH crystalline flakes were prepared through direct pyrolysis of hickory wood chips and aluminum salt activation [17].

The EDX analysis before and after adsorption (Fig. 2c) clearly shows the main components of PMB, namely carbon, oxygen, and iron. This suggests that the iron salt has transformed into ferric oxide within the porous carbon structure during the second-stage pyrolysis. After the adsorption, a phosphate peak appears on the graph, while

the intensity of the iron peak reduces. This confirms that phosphate is bonded to the ferric sites within the carbon structure.

The XRD patterns (Fig. 2d) show the main diffraction peaks. Peaks located at  $2\theta$  values of  $26^\circ$ ,  $43^\circ$ ,  $44^\circ$  are related to carbon, which suggests that biomass has transformed to graphite, and peaks at  $30^\circ$  and  $35^\circ$  are diffraction pattern characteristics of magnetite  $\text{Fe}_3\text{O}_4$  or  $\text{Fe}_2\text{O}_3$ . XRD patterns of the biochars before and after adsorption show minimal differences. The intensity of the peaks at  $43^\circ$  and  $44^\circ$  is reduced, which is an indication of phosphate adsorption on the active ferric sites and a minor change of the crystalline structure of the adsorbent.

The average crystallite size ( $L$ ) was calculated based on Scherrer Eq. (3) with Origin Curve Fitting.

$$L = \frac{K\lambda}{\beta \cos \theta}, \quad (3)$$

where  $K$  is the Scherrer constant (0.9),  $\lambda$  is the X-ray wavelength (0.15406 nm),  $\beta$  is the full width at half maximum of the peak (radians), and  $\theta$  is the diffraction angle (radians). Crystallinity ( $X$ ) was also determined as:

$$X(\%) = \frac{A_c}{A_{c+am}} \times 100, \quad (4)$$

where  $A_c$  is the area under the crystalline peaks and  $A_{c+am}$  is the area under the crystalline peaks plus the amorphous area. The values for  $L$  and  $X$  were 23.1 nm and 45% before adsorption, which changed to 14.1 nm and 40%, respectively, after adsorption. This indicates that the reaction of phosphate with the iron oxide crystals in the biochar structure forms a smaller average crystallite size with a lower degree of crystallinity, which is also observed in the SEM images in Fig. 2a and b.

The FTIR spectra of the PMB and reference biochar (R6) before and after phosphate adsorption are given in Fig. 2e. The band at  $2150 \text{ cm}^{-1}$  related to  $\text{C}\equiv\text{C}$  can be found in both biochars. The reference biochar has no difference before and after phosphate adsorption, showing the same peaks. Two large peaks at  $1570 \text{ cm}^{-1}$  and  $1200 \text{ cm}^{-1}$  are related to  $\text{C}=\text{C}$  stretching and  $\text{C}-\text{O}$  stretching, respectively. On the contrary, several differences can be found for the PMB before and after adsorption. PMB before adsorption shows a peak at  $1020 \text{ cm}^{-1}$ , which is related to out-of-plane  $\text{C}-\text{H}$  bending, and the peak at  $730 \text{ cm}^{-1}$ . This peak corresponds to the  $\text{C}-\text{Cl}$  band, meaning that not all Cl was washed from the biochar. After the adsorption, bands at  $2980 \text{ cm}^{-1}$  and  $2880 \text{ cm}^{-1}$  can be found, indicating asymmetric and symmetric  $\text{C}-\text{H}$ . Also, the spectrum of the spent adsorbent indicates numerous moderate bands in the range between  $1380$  and  $930 \text{ cm}^{-1}$  related to  $\text{P}=\text{O}$  and  $\text{P}-\text{O}$  compounds, which confirms the phosphate adsorption



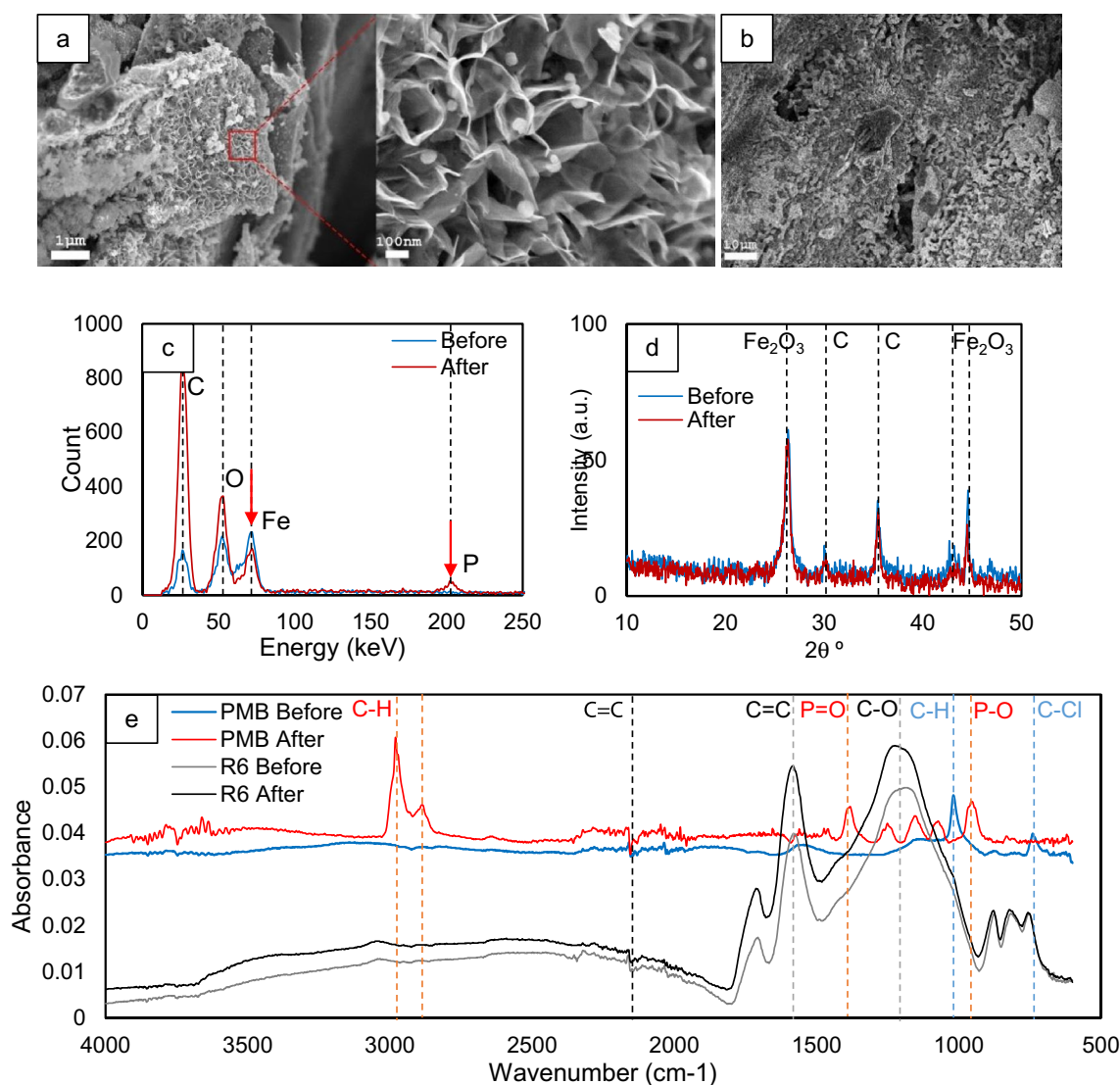


**Fig. 2** Magnetic biochar characterization (sample A2); **a** SEM images of the biochar at the nano- and micro-scales before adsorption; **b** SEM image of the biochar after adsorption; **c** EDX spectra of the bio-

char before and after adsorption; **d** XRD profile of biochar before and after adsorption; **e** FT-IR spectra of the reference biochar (R6) and PMB before and after adsorption

[20, 21]. These bonds related to phosphate also support EDX data indicating phosphate attachment on the biochar surface after adsorption.

While the pristine biochar (R6) showed 571 m<sup>2</sup>/g of specific surface area and 0.025 cm<sup>3</sup>/g pore volume, the developed biochar showed 94 m<sup>2</sup>/g and 0.002 cm<sup>3</sup>/g. As it is observed in the SEM images, ferric-oxide particles are present within a honeycomb-like porous carbon structure, which can somewhat consume the surface area and volume. These particles further act as active sites for complexation with phosphate. Therefore, the removal mechanisms involved in phosphate adsorption benefit from both porosity and active sites. The adsorption mechanism and

the porous structure can be explained with the shape of the nitrogen gas adsorption–desorption isotherm, presented in Fig. 3a. A hysteresis loop emerged on the isotherm curve at a high relative pressure region indicating a type IV behavior and a wide mesopore distribution in the developed biochar [22]. The pore size distribution (PSD) of the developed biochar and pristine biochar is given in Fig. 3b. As seen, in both cases the PSD is within the 2–50 nm range. For the biochar R6 pores are mostly in the range of 3–4 nm and the pores of PMB are distributed more equally in a mesoporous area with an average pore diameter of 10 nm.

**Fig. 3** Comparison of PMB (A2) to reference biochar (R6). **a** Nitrogen adsorption–desorption isotherm; **b** Pore size distribution

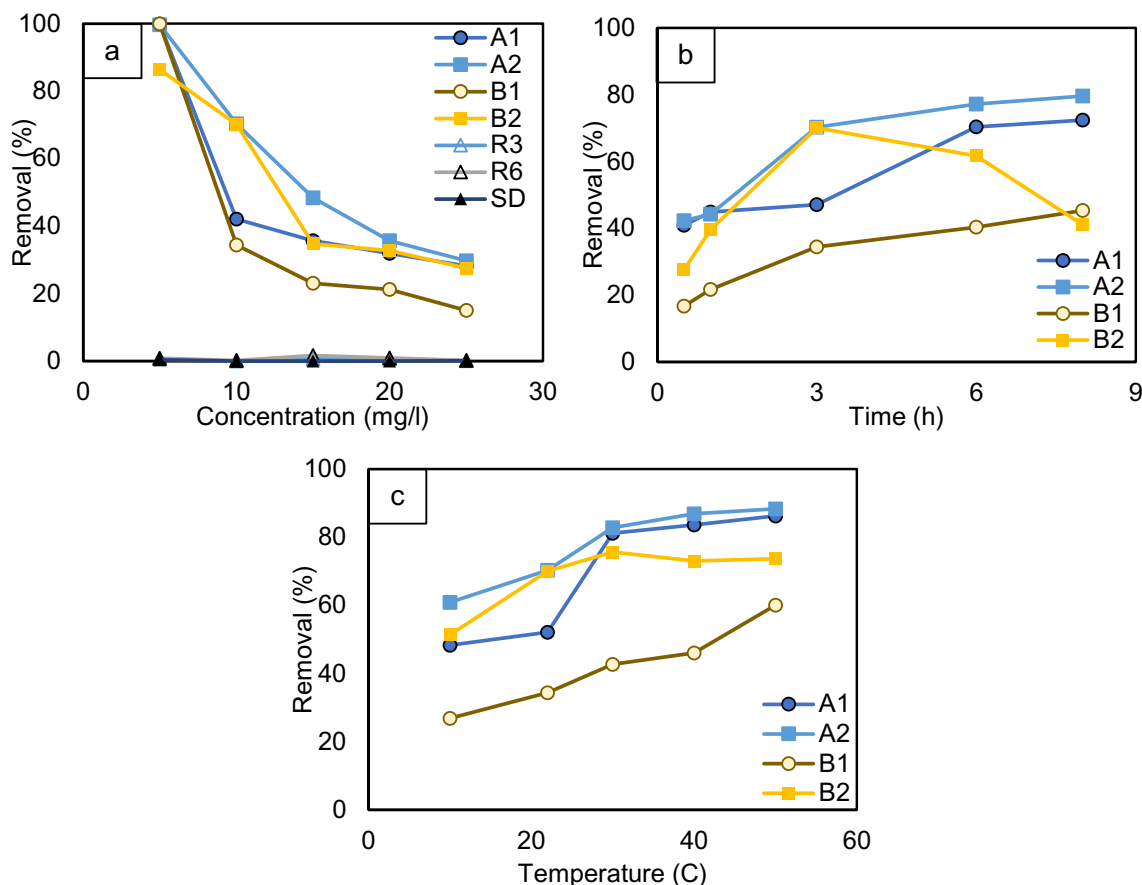
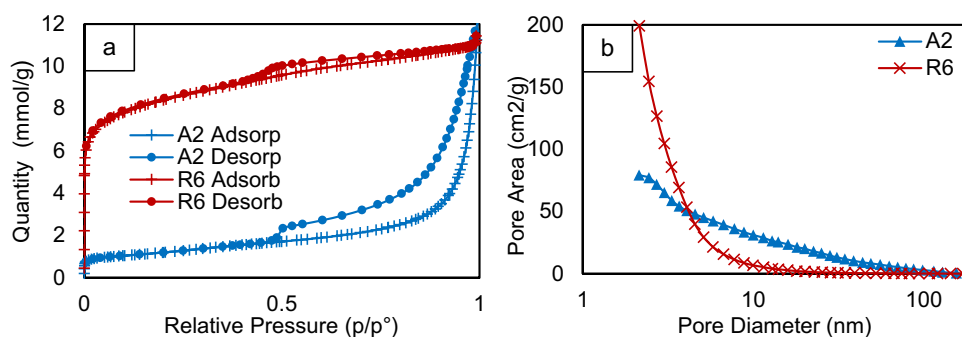


**Fig. 4** Adsorption results: **a** Removal percentage of phosphate by magnetic biochars at different initial concentrations (upon 3 h of contact time and room temperature); **b** Removal percentage at different

contact times (initial concentration 10 mg/l P and room temperature); **c** Removal percentage at different temperatures (initial concentration 10 mg/l P and contact time 3 h)

### 3.2 Phosphate adsorption

The phosphate adsorption efficiency was tested in the batch mode and the results are illustrated in Fig. 4. The dependence of phosphate removal to initial phosphate concentration in water is presented in Fig. 4a. The pristine reference biochars (without activation, R3, and R6), as well as the biomass sawdust (SD), were incapable of phosphate uptake. On the other hand, all PMBs showed highly effective removal

of phosphate. At lower concentrations (5 mg/l P), the PMBs A1, A2, B1 were able to reach complete (100%) phosphate removal and biochar B2 reached 86%. At the highest studied concentration (25 mg/l P) the biochar A2 showed the highest removal performance at 30%, while samples A1 and B2 reached around 25% removal. Therefore, the PMB A2 was identified as the best sample for the effective adsorption process, which was produced via 200 °C first-step pyrolysis, iron salt activation, and 800 °C second-step pyrolysis

procedure. The inability of phosphate uptake by the pristine biochars confirms the necessity of their modification to provide adsorptive functional groups for effective phosphate adsorption. These results suggest that the removal mechanisms involve a combination of electrostatic adsorption, co-precipitation, and complexation on the surface and within the structure of the functionalized solid adsorbent [23]. Thus, further experiments do not include the reference biochars.

The effect of contact time, which is an essential parameter for the adsorption process, was also studied and results are shown in Fig. 4b. A similar trend is noticeable for biochars A1, A2, and B1; the removal of phosphate gradually grows with the contact time. The biochar B2 showed a decrease in removal from 70 to 41% after 3 h up to 8 h of contact time. This suggests that extra time of reaction may lead to undesired desorption of the pollutant back to the water. The best-performed biochar was A2, which showed 70% of removal after 3 h of contact time and 79% after 8 h of contact time. The lowest removal was observed with PMB B1, with 34% and 45% at 3 and 8 h of contact time, respectively. Therefore, 3 h contact time was selected as the optimum process time to achieve desirable removal efficacy as well as to save energy and time. The experimental data showed a good fit to the pseudo-second-order kinetic model in the following equation ( $r^2=0.97$ ). This is indicative of chemisorption, common for phosphate adsorption, which is controlled by the adsorbent and the adsorbate characteristics [24].

$$\frac{t}{q_t} = \frac{1}{kq_e^2} + \frac{t}{q_e}, \quad (5)$$

where  $t$  is the contact time (min). The rate constant  $k$  and the equilibrium uptake  $q_e$  were 0.003 g/mg min and 6.16 mg/g, respectively.

The effect of the solution temperature on phosphate removal is shown in Fig. 4c. The removal increases upon the temperature increase. The removal by biochar samples A1, A2, and B2 showed a high dependency on the water temperature. The removal increased from around 50% at 10 °C to 88% at 50 °C. The least temperature dependency was observed for sample B1 with 27% removal at 10 °C which increased to 60% at 50 °C. This shows the endothermic nature of the adsorption process. The temperature affects the adsorption process by increasing the diffusion rate within the boundary layer, i.e. the resistance to the external mass transfer, and the pores as well as by changing the equilibrium capacity of the adsorbent for the target adsorbate [25]. The mass transfer through the boundary layer thickness or by the intra-particle diffusion typically dominate the adsorptive uptake of solutes from liquids.

Considering the obtained adsorption results, the PMBs produced under 200 °C at the first step of pyrolysis

performed better than the ones produced under 300 °C. The biochar A2 showed the best adsorption performance and as such was selected for further analysis and characterization.

Isotherm study can shed light upon further surface characteristics of the PMB. The two most-used isotherms—Langmuir (Eq. 6) and Freundlich (Eq. 7) models were employed to understand the nature of phosphate adsorption on the best performing biochar (A2).

$$\frac{C_e}{q_e} = \frac{C_e}{q_L} + \frac{1}{q_L K_L} \quad (6)$$

$$\log(q_e) = \log(K_F) + \frac{1}{n} \log(C_e), \quad (7)$$

where  $q_L$  is the monolayer capacity and  $K_L$  is the equilibrium constant for the Langmuir model which assumes a monolayer coverage of the adsorbate at specific homogeneous active sites of the adsorbent [26]. On the other hand, the Freundlich model considers multilayer coverage for adsorption onto a heterogeneous adsorbent surface [27].  $K_F$  is the Freundlich coefficient and  $1/n$  constant indicating the adsorption intensity and surface heterogeneity. The isotherm was investigated under five phosphate concentrations at room temperature and in neutral pH (around 6.5), where phosphate exists as a combination of  $\text{H}_2\text{PO}_4^-$  and  $\text{HPO}_4^{2-}$  species [28]. The calculated values are tabulated in Table 1 and the models are plotted in Fig. 5a and b.

The adsorption onto the biochar A2 followed the Langmuir model ( $R^2=0.99$ ) better than the Freundlich model (0.88). This further indicates the presence of specific active ferric sites enabling a monolayer phosphate coverage on the surface. Previously, a Langmuir monolayer coverage of chromium was also observed for corncob-derived magnetic biochar [29]. A brief comparison of phosphate adsorption with different porous materials is given in Table 2. The adsorption capacity of PMB is comparable to the other previously reported materials such as biochar from different source biomass [30], iron oxide coated sand [31], and activated carbon [32]. Worth noting that the adsorption operational parameters need to be considered when comparing the adsorptive performance of different materials.

**Table 1** The calculated values of the Langmuir and Freundlich isotherms

Langmuir			Freundlich		
$K_L$ (L/mg)	$q_L$ (mg/g)	$R^2$	$K_F$ (mg/g $\cdot$ (L/mg) $^{1/n}$ )	$1/n$	$R^2$
0.01	3.47	0.99	1.63	0.05	0.88



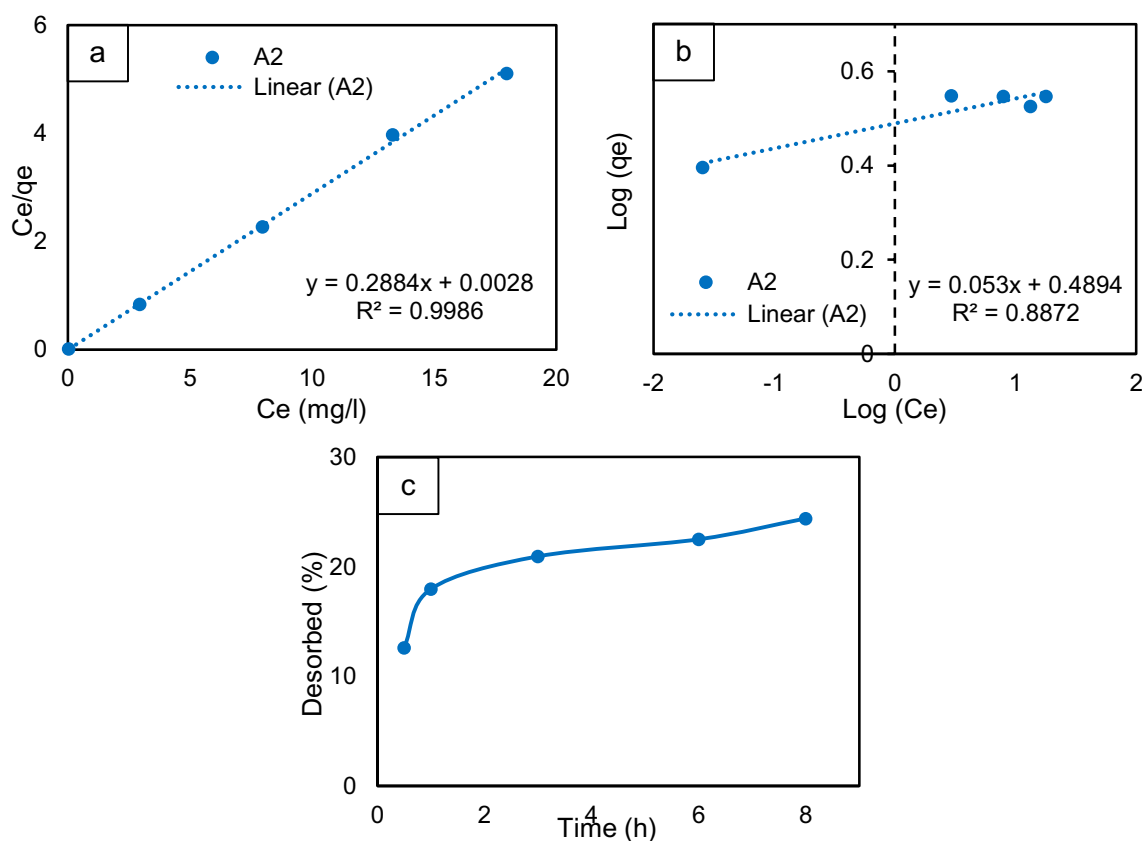


**Fig. 5** **a** Linear Langmuir and **b** Freundlich isotherm **c** Desorption of the phosphate over time from sample A2 into the acidic water (pH 2)

**Table 2** Phosphate adsorption on different porous adsorbents; a comparison based on Langmuir maximum adsorption capacity at room temperature

Adsorbents	Adsorption (mg/g)	Kinetic model fit	Reference
Porous magnetic biochar	3.47	Pseudo-second order	Present work
Iron oxide coated sand	0.88–1.50	Not determined	[33]
Lanthanum-loaded granular ceramics	0.85	Pseudo-second order	[31]
Industrial solid waste-based biochar	3.20	Pseudo-second order	[30]
Zn-chitosan complexation	6.3	Pseudo-second order	[24]
ZnCl <sub>2</sub> -activated carbon	5.1	Pseudo-second order	[32]

### 3.3 Desorption

The desorption study resulted in the release of the adsorbed phosphate into an acidic solution, as can be seen in Fig. 5c. During the prior adsorption stage, 23.6% was adsorbed from the 25 mg/l phosphate solution, which is consistent with the concentration study. After half an hour of desorption time, the release was 17% and reached 24% after 8 h. However, the next resorption stage on the desorbed biochar showed only 3.8% of phosphate uptake. The third resorption during the third cycle reached 3%. This indicates that the main involved adsorption mechanism is the complexation of phosphate with iron oxides embedded within the biochar structure, which is consistent with isotherm and XRD analyses.

The complexes, formed during the first cycle, may not be easily broken and as such may leave the carbon structure as iron-P complex to the next phase. Moreover, long exposure to a strongly acidic environment facilitates the iron release in the complex from the carbon structure. Nevertheless, slow desorption is present as a viable solution for the reuse of P-loaded biochar, enabling the reclamation of phosphorous. In this case, it is reasonable to reuse the loaded adsorbent as a slow-release fertilizer to improve the soil elemental composition and fertility [23, 34]. Zheng et al. reclaimed P from secondary treated wastewater by biochar loaded with aluminum oxyhydroxides (AlOOH). The P-loaded biochar was then used as growth media for mung bean germination and seedling growth and compared with a sand-based growth

media. The seed germination rate was increased from 30% in sole sand to 46.7% in the sand together with P-loaded biochar [17]. Thus, engineered biochars are promising media for P-reclamation from wastewater treatment plants as value-added fertilizers, which is a sustainable environmental strategy for the mitigation of eutrophication, the enhancement of soil quality, the sequestration of carbon, and the recycling of phosphorus.

The complexation between the phosphate and the iron active sites on the PMB is schematically shown in Fig. 6a. Phosphate ions usually form inner-sphere complexation with different metal-based compounds such as the iron oxides, embedded within the porous carbon structure, which is consistent with the chemisorption shown in the kinetic, isotherm, desorption analyses.

### 3.4 Magnetization

The separation process of adsorbent, especially in the fine powdered form such as powdered AC, from treated water requires additional energy. Usually, the intensive filtration step is used to avoid secondary pollution with the carbon particles. Such additional steps consequently increase the costs of treatment. Therefore, additional magnetic properties can facilitate the separation of the used adsorbent particles from the water phase via a magnetic field when used in powdered form. It was reported that high pyrolysis temperature enhances the magnetic properties by converting the ferric ions to ferric oxide within the graphitic structure [29, 35]. Thus, the magnetic properties of developed PMBs were tested on sample A2. The results of the VSM analysis, shown in Fig. 6b, revealed that the magnetic strength of PMBs is 38.9 emu/g and that PMBs have properties of a superparamagnetic material. After the phosphate adsorption, the magnetic strength decreased to 28.4 emu/g. Such a decrease can be caused by the complexation of ferric oxide with adsorbed phosphorous. Despite the decrease, PMB remains magnetically active and can be easily separated

from the aqueous solution with a magnet as shown on the up left picture in Fig. 6b. Magnetization of magnetic biochar derived from corncobs and peanut hulls under different pyrolysis temperatures was reported to range from 11.27 to 26.20 emu/g, which were used for chromium adsorption and separation [29]. Powdered AC magnetized by iron oxide magnetic nanoparticles was reported with a magnetic strength of 51.5 emu/g, which was used as a magnetic adsorbent for ciprofloxacin antibiotics [36].

## 4 Conclusion

In this study, highly PMBs were produced through activation of low-temperature-derived biochar with iron salt and second-step pyrolysis at a higher temperature. Four temperature combinations were used during the production stage. The optimal production parameters were identified by testing the developed adsorbent for phosphate adsorption. The best performing biochar was produced at 200 °C first-step pyrolysis temperature and 800 °C second-step pyrolysis temperature after activation. SEM/EDX, FTIR, XRD, and BET analyses were used to investigate the structural and compositional characteristics of the developed biochars. The characterization confirmed the presence of embedded ferric oxide particles with 23 nm average crystallite size within the hierarchical porous carbon structure, which can act as active sites for effective phosphate uptake. The effect of phosphate concentration, water temperature, and process time on the adsorption of phosphate was explored in batch mode. The increase in process time and temperature favored the adsorption. At 5 mg/l P concentration, the PMBs A1, A2, and B1 were able to reach complete phosphate removal and biochar B2 reached 86%, while at 25 mg/l P concentration, the biochar B1 showed 14% removal and other PMBs reached around 30% removal. The adsorption followed Langmuir isotherm and pseudo-second-order kinetic model and was endothermic chemisorption in nature. PMBs showed

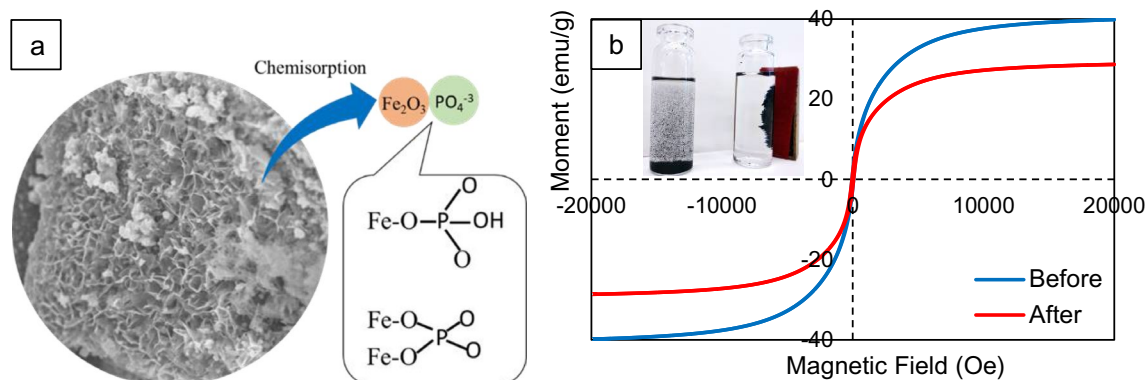


**Fig. 6** **a** A schematic representation of removal mechanism, **b** a magnetization curve of developed PMB

38.9 emu/g magnetic strength and can be easily separated from water with aid of a magnetic field to be reused as slow-release fertilizers after phosphate adsorption. These results portrait the produced PMBs as a promising adsorbent for phosphate removal and reclaim.

**Acknowledgements** The authors thank Professor Riku Vahala for his valuable comments. We made use of OtaNano Nanomicroscopy Center (NMC) and Bioeconomy and RawMatters research infrastructures.

**Author contributions** Both authors contributed to the study equally.

**Funding** Open Access funding provided by Aalto University. This research was funded by Aalto University Doctoral Programme for Engineering (D/23/00.01.02.00/2019), Maa ja vesitekniiikan tuki ry (Grant 388823), and the Academy of Finland (343192).

**Data availability** All data and materials comply with field standards.

**Code availability** Not applicable.

## Declarations

**Conflict of interest** The authors declare that they have no known competing financial interest or personal relationships that could have appeared to influence the work reported in this paper.

**Open Access** This article is licensed under a Creative Commons Attribution 4.0 International License, which permits use, sharing, adaptation, distribution and reproduction in any medium or format, as long as you give appropriate credit to the original author(s) and the source, provide a link to the Creative Commons licence, and indicate if changes were made. The images or other third party material in this article are included in the article's Creative Commons licence, unless indicated otherwise in a credit line to the material. If material is not included in the article's Creative Commons licence and your intended use is not permitted by statutory regulation or exceeds the permitted use, you will need to obtain permission directly from the copyright holder. To view a copy of this licence, visit <http://creativecommons.org/licenses/by/4.0/>.

## References

1. M.R. Yazdani et al., Tailored mesoporous biochar sorbents from pinecone biomass for the adsorption of natural organic matter from lake water. *J. Mol. Liq.* **291**, 111248 (2019). <https://doi.org/10.1016/j.molliq.2019.111248>
2. T. Tsubota, M. Morita, S. Kamimura, T. Ohno, New approach for synthesis of activated carbon from bamboo. *J. Porous Mater.* **23**(2), 349–355 (2016). <https://doi.org/10.1007/s10934-015-0087-6>
3. O. Tomin, R. Vahala, M.R. Yazdani, Tailoring metal-impregnated biochars for selective removal of natural organic matter and dissolved phosphorus from the aqueous phase. *Microporous Mesoporous Mater.* **328**, 111499 (2021). <https://doi.org/10.1016/j.micromeso.2021.111499>
4. X. Fan, Z. Qian, J. Liu, N. Geng, J. Hou, D. Li, Investigation on the adsorption of antibiotics from water by metal loaded sewage sludge biochar. *Water Sci. Technol.* (2020). <https://doi.org/10.2166/wst.2020.578>
5. H. Deng et al., Removal of Zn(II), Mn(II) and Cu(II) by adsorption onto banana stalk biochar: adsorption process and mechanisms. *Water Sci. Technol.* **82**(12), 2962–2974 (2020). <https://doi.org/10.2166/wst.2020.543>
6. H.S. Kambo, A. Dutta, A comparative review of biochar and hydrochar in terms of production, physico-chemical properties and applications. *Renew. Sustain. Energy Rev.* **45**, 359–378 (2015). <https://doi.org/10.1016/j.rser.2015.01.050>
7. T. Sizmur, T. Fresno, G. Akgül, H. Frost, E. Moreno-Jiménez, Biochar modification to enhance sorption of inorganics from water. *Bioresour. Technol.* **246**, 34–47 (2017). <https://doi.org/10.1016/j.biortech.2017.07.082>
8. Y. Zhou et al., Modification of biochar derived from sawdust and its application in removal of tetracycline and copper from aqueous solution: adsorption mechanism and modelling. *Bioresour. Technol.* **245**, 266–273 (2017). <https://doi.org/10.1016/j.biortech.2017.08.178>
9. J.S. Cha et al., Production and utilization of biochar: a review. *J. Ind. Eng. Chem.* **40**, 1–15 (2016). <https://doi.org/10.1016/j.jiec.2016.06.002>
10. M. Ahmad et al., Biochar as a sorbent for contaminant management in soil and water: a review. *Chemosphere* **99**, 19–33 (2014). <https://doi.org/10.1016/j.chemosphere.2013.10.071>
11. M. Plötze, P. Niemz, Porosity and pore size distribution of different wood types as determined by mercury intrusion porosimetry. *Eur. J. Wood Wood Prod.* **69**(4), 649–657 (2011). <https://doi.org/10.1007/s00107-010-0504-0>
12. S. Jiang et al., Characterization of hard- and softwood biochars pyrolyzed at high temperature. *Environ. Geochem. Health* **39**(2), 403–415 (2017). <https://doi.org/10.1007/s10653-016-9873-6>
13. J. Némery, J. Garnier, The fate of phosphorus. *Nat. Geosci.* (2016). <https://doi.org/10.1038/ngeo2702>
14. M.N. Khan, F. Mohammad, Eutrophication: challenges and solutions, in *Eutrophication: causes, consequences and control*, vol. 2, ed. by A.A. Ansari, S.S. Gill (Springer, Dordrecht, 2014), pp. 1–15. [https://doi.org/10.1007/978-94-007-7814-6\\_1](https://doi.org/10.1007/978-94-007-7814-6_1)
15. J.T. Bunce, E. Ndam, I.D. Ofiteru, A. Moore, D.W. Graham, A review of phosphorus removal technologies and their applicability to small-scale domestic wastewater treatment systems. *Front. Environ. Sci.* (2018). <https://doi.org/10.3389/fenvs.2018.00008>
16. S. Kilpimaa, H. Runtti, T. Kangas, U. Lassi, T. Kuokkanen, Physical activation of carbon residue from biomass gasification: novel sorbent for the removal of phosphates and nitrates from aqueous solution. *J. Ind. Eng. Chem.* **21**, 1354–1364 (2015). <https://doi.org/10.1016/j.jiec.2014.06.006>
17. Y. Zheng et al., Reclaiming phosphorus from secondary treated municipal wastewater with engineered biochar. *Chem. Eng. J.* **362**, 460–468 (2019). <https://doi.org/10.1016/j.cej.2019.01.036>
18. O. Mašek, P. Brownsort, A. Cross, S. Sohi, Influence of production conditions on the yield and environmental stability of biochar. *Fuel* **103**, 151–155 (2013). <https://doi.org/10.1016/j.fuel.2011.08.044>
19. M.J. Antal Jr., M. Grønli, The art, science, and technology of charcoal production. *Ind. Eng. Chem. Res.* **42**(8), 1619–1640 (2003). <https://doi.org/10.1021/ie0207919>
20. E. Apaydın-Varol, A.E. Pütün, Preparation and characterization of pyrolytic chars from different biomass samples. *J. Anal. Appl. Pyrolysis* **98**, 29–36 (2012). <https://doi.org/10.1016/j.jaap.2012.07.001>
21. P. Larkin, *Infrared and Raman spectroscopy: principles and spectral interpretation* (Elsevier, Saint Louis, 2011)
22. D. Xia et al., ZnCl<sub>2</sub>-activated biochar from biogas residue facilitates aqueous As(III) removal. *Appl. Surf. Sci.* **377**, 361–369 (2016). <https://doi.org/10.1016/j.apsusc.2016.03.109>
23. Y. Yi et al., Magnetic biochar for environmental remediation: a review. *Bioresour. Technol.* **298**, 122468 (2020). <https://doi.org/10.1016/j.biortech.2019.122468>

24. M.R. Yazdani, E. Virolainen, K. Conley, R. Vahala, Chitosan–zinc(II) complexes as a bio-sorbent for the adsorptive abatement of phosphate: mechanism of complexation and assessment of adsorption performance. *Polymers* **10**, 25 (2018)
25. M.R. Yazdani, T. Tuutijärvi, A. Bhatnagar, R. Vahala, Adsorptive removal of arsenic(V) from aqueous phase by feldspars: kinetics, mechanism, and thermodynamic aspects of adsorption. *J. Mol. Liq.* **214**, 149–156 (2016). <https://doi.org/10.1016/j.molliq.2015.12.002>
26. M.R. Yazdani, A. Bhatnagar, R. Vahala, Synthesis, characterization and exploitation of nano-TiO<sub>2</sub>/feldspar-embedded chitosan beads towards UV-assisted adsorptive abatement of aqueous arsenic (As). *Chem. Eng. J.* **316**, 370–382 (2017). <https://doi.org/10.1016/j.cej.2017.01.121>
27. H. Freundlich, Über die Adsorption in Lösungen. *Z. Für Phys. Chem.* **57U**(1), 385–470 (1907). <https://doi.org/10.1515/zpch-1907-5723>
28. B. da Silva Cerozi, K. Fitzsimmons, The effect of pH on phosphorus availability and speciation in an aquaponics nutrient solution. *Bioresour. Technol.* **219**, 778–781 (2016). <https://doi.org/10.1016/j.biortech.2016.08.079>
29. O. Xin, H. Yitong, C. Xi, C. Jiawei, Magnetic biochar combining adsorption and separation recycle for removal of chromium in aqueous solution. *Water Sci. Technol.* **75**(5), 1177–1184 (2017). <https://doi.org/10.2166/wst.2016.610>
30. B. Qiu, F. Duan, Synthesis of industrial solid wastes/biochar composites and their use for adsorption of phosphate: From surface properties to sorption mechanism. *Colloids Surf. Physicochem. Eng. Asp.* **571**, 86–93 (2019). <https://doi.org/10.1016/j.colsurfa.2019.03.041>
31. N. Chen et al., Preparation and characterization of lanthanum(III) loaded granular ceramic for phosphorus adsorption from aqueous solution. *J. Taiwan Inst. Chem. Eng.* **43**(5), 783–789 (2012). <https://doi.org/10.1016/j.jtice.2012.04.003>
32. C. Namasivayam, D. Sangeetha, Equilibrium and kinetic studies of adsorption of phosphate onto ZnCl<sub>2</sub> activated coir pith carbon. *J. Colloid Interface Sci.* **280**(2), 359–365 (2004). <https://doi.org/10.1016/j.jcis.2004.08.015>
33. N. Boujelben, J. Bouzid, Z. Elouear, M. Feki, F. Jamoussi, A. Montiel, Phosphorus removal from aqueous solution using iron coated natural and engineered sorbents. *J. Hazard. Mater.* **151**(1), 103–110 (2008). <https://doi.org/10.1016/j.jhazmat.2007.05.057>
34. S. Jeffery, F.G.A. Verheijen, M. van der Velde, A.C. Bastos, A quantitative review of the effects of biochar application to soils on crop productivity using meta-analysis. *Agric. Ecosyst. Environ.* **144**(1), 175–187 (2011). <https://doi.org/10.1016/j.agee.2011.08.015>
35. X. Zhang, Z. Ou, J. Xiang, Fabrication of magnetic activated carbon from waste macroporous resin via Fenton's reagent impregnation. *J. Porous Mater.* **28**(1), 165–170 (2021). <https://doi.org/10.1007/s10934-020-00980-3>
36. T.J. Al-Musawi, A.H. Mahvi, A.D. Khatibi, D. Balarak, Effective adsorption of ciprofloxacin antibiotic using powdered activated carbon magnetized by iron(III) oxide magnetic nanoparticles. *J. Porous Mater.* **28**(3), 835–852 (2021). <https://doi.org/10.1007/s10934-021-01039-7>

**Publisher's Note** Springer Nature remains neutral with regard to jurisdictional claims in published maps and institutional affiliations.